Petroleum Science 20 (2023) 827–839

Contents lists available at ScienceDirect

Petroleum Science

journal homepage: www.keaipublishing.com/en/journals/petroleum-science

Original Paper

Solving elastic wave equations in 2D transversely isotropic media by a weighted Runge-Kutta discontinuous Galerkin method

Xi-Jun He [a], Jing-Shuang Li [b, *], Xue-Yuan Huang [a], Yan-Jie Zhou [a]

[a] School of Mathematics and Statistics, Beijing Technology and Business University (BTBU), Beijing, 100048, China
[b] School of Science, China University of Mining and Technology (Beijing), Beijing, 100083, China

ARTICLE INFO

Article history:
Received 19 May 2022
Received in revised form
19 August 2022
Accepted 13 October 2022
Available online 17 October 2022

Edited by Jie Hao

Keywords:
Discontinuous Galerkin method
Anisotropy
Transversely isotropic
Modeling

ABSTRACT

Accurate wave propagation simulation in anisotropic media is important for forward modeling, migration and inversion. In this study, the weighted Runge-Kutta discontinuous Galerkin (RKDG) method is extended to solve the elastic wave equations in 2D transversely isotropic media. The spatial discretization is based on the numerical flux discontinuous Galerkin scheme. An explicit weighted two-step iterative Runge-Kutta method is used as time-stepping algorithm. The weighted RKDG method has good flexibility and applicability of dealing with undulating geometries and boundary conditions. To verify the correctness and effectiveness of this method, several numerical examples are presented for elastic wave propagations in vertical transversely isotropic and tilted transversely isotropic media. The results show that the weighted RKDG method is promising for solving wave propagation problems in complex anisotropic medium.

1. Introduction

Transversely isotropic (TI) medium is an effective elastic approximation to describe the cracks and thin interbeds widely existing in underground rocks. In actual seismic exploration, most of the sedimentary rocks are TI medium. Thomsen (1986) systematically analyzed the group and phase velocities in TI media, and introduced the Thomsen coefficients to represent the anisotropic characteristics of the medium. The TI medium has a symmetry axis, and the seismic wave propagation in the plane perpendicular to the symmetry axis has isotropic behaviors. According to the position of the symmetry axis, the TI media fall into three categories: vertical TI (VTI), horizontal TI (HTI) and tilted TI (TTI). The VTI media are mainly composed of periodic thin layer, the HTI media are generally oriented cracks or fissures arranged in parallel, and the TTI media are generally inclined cracks.

Studying the seismic wave propagation in anisotropic media is of great significance for understanding the propagation laws of seismic waves and interpreting seismic data (Carcione, 2007; Wu et al., 2010; Fletcher et al., 2009). In actual seismic exploration, due to the complexity and inhomogeneity of the underground medium, there are few models that we can obtain analytical solutions for the propagation of seismic wavefields. Therefore, it is extremely important to study the numerical solutions. When numerically solving the wave equation, due to different mathematical theories and discretization methods based on the discretization process, many numerical calculation methods have been suggested including the finite-difference method (FDM) (e.g., Igel et al., 1995; Hestholm, 1999; Moczo et al., 2000; Gao and Zhang, 2006; Yang et al., 2007; Du et al., 2009; Liu and Sen, 2009; Sun et al., 2016; Wang et al., 2016; Wang et al., 2019; Sethi et al., 2022), the finite element method (FEM) (Carcione et al., 2011; Moczo et al., 2011), the pseudo-spectral method (PSM) (Nielsen et al., 1994), and the spectral element method (SEM) (e.g., Komatitsch et al., 1999; Xu et al., 2021).

Topographies are often encountered in practical scenarios. Some are irregular regional boundaries such as undulating surface, and some are special structures such as fractures and small holes which are commonly found in unconventional oil and gas exploration. In view of these situations, the conventional FDM needs to adopt the staircase method. But the staircase method is complicated to program, and it tends to generate false diffraction waves at the region boundary. However, if we use the traditional FEM, although the mesh can be divided flexibly, FEM requires a large amount of

* Corresponding author.
E-mail address: lijingshuang322@126.com (J.-S. Li).

https://doi.org/10.1016/j.petsci.2022.10.007

calculation and is not easy to parallelize. Many geophysicists have proposed a series of effective methods to tame the topographic surfaces (e.g., Hestholm and Ruud, 2002; Gao and Zhang, 2006; Lan and Zhang, 2011; Zhang et al., 2012; Shragge, 2014; Sun et al., 2016; Rao and Wang, 2019). Especially, Gao and Zhang (2006) solved the 3D elastic wave propagation problems in anisotropic media using a parallel grid method, which uses a mixed mesh of tetrahedrons and parallelepipedons to approximate arbitrary 3D topographies. Lan and Zhang (2011) suggested a finite-difference approach to solve wave propagations in 3D heterogeneous TI media. They implement the surface topography by a mapping between rectangular grids and curved grids, and they verified the efficiency of this method by performing efficient tests. Zhang et al. (2012) proposed a collocated-grid method on curvilinear grids for elastic wave modelling, afterwards, Sun et al. (2016, 2018) extended this method to simulate 2D and 3D elastic wavefields in general anisotropic media, respectively. Rao and Wang (2019) carried out detailed analyses on the numerical stability and dispersion for the pseudo-acoustic wave equation in TTI medium. To deal with the surface or interface topographies, they mapped the nonrectangular quadrilateral grids to the quadrangle grids in Cartesian coordinates, and then implemented the simulations using FDM.

The discontinuous Galerkin (DG) method is a popular method that has been increasingly applied in the past decade. A series of DG methods have been developed and widely used in many fields (e.g., Reed and Hill, 1973; Cockburn and Shu, 1989; Hu et al., 1999; Cockburn and Shu, 2001; Hesthaven and Warburton, 2007). The DG method has also found many applications in geosciences (e.g., Käser and Dumbser, 2006; Patra et al., 2006; de la Puente et al., 2007; Levy et al., 2007; Rivière, 2008; de Basabe et al., 2016; Modave et al., 2016; Yang et al., 2016; Clare et al., 2020; He et al., 2019a, 2019b, 2020a, 2020b; Qiu et al., 2020; Huang et al., 2022). The DG method has many positive features such as the flexibility on dealing with complex structure and boundary conditions; in particular, it is convenient to handle free surface boundary conditions. Moreover, the solutions on each element are independent, and they are connected by numerical fluxes at element boundaries, leading to good parallelism. We should point out that, the SEM and DG methods have many similarities, for examples, they are both variants of FEM, they can handle complex boundaries and have high accuracy, and the mass matrices can be diagonal or block diagonal. But SEM usually uses quadrilateral and hexahedral meshes, which are difficult to deal with severe surface fluctuations. Although SEM can now successfully apply triangular and tetrahedral meshes, the mass matrices are no longer diagonal, which increase the programming difficulty and computational cost. However, the DG method is flexible and convenient to use triangular or tetrahedral meshes.

In this study, we extend the weighted RKDG method to simulate wave propagations in 2D TI media. An explicit weighted two-step iterative Runge-Kutta method is used as time-stepping algorithm, and the spatial discretization is based on the DG formulations using the local Lax-Friedrichs numerical flux. We first outline the wave equations for general anisotropic media. Then, the weighted RKDG scheme will be stated, with the notice to deal with boundaries. Some numerical examples are finally provided to validate this method.

2. Governing equations

The source-free elastic wave equation is given by (Aki and Richards, 2002):

$$\rho \frac{\partial \mathbf{V}}{\partial t} = \nabla \cdot \boldsymbol{\sigma}, \tag{1}$$

in which $\mathbf{V} = (v_x, v_y, v_z)^T$ is the velocity vector, $\boldsymbol{\sigma}$ is the stress tensor, $\rho = \rho(x, y, z)$ is the density, and $\nabla = (\partial_x, \partial_y, \partial_z)$ denotes the gradient operator. Here, the divergence operator "$\nabla\cdot$" is implemented on each row of $\boldsymbol{\sigma}$. According to Hooke's law, the stress-strain constitutive relationship is:

$$\begin{pmatrix} \sigma_{xx} \\ \sigma_{yy} \\ \sigma_{zz} \\ \sigma_{yz} \\ \sigma_{xz} \\ \sigma_{xy} \end{pmatrix} = \mathbf{C}\boldsymbol{\varepsilon} = \begin{pmatrix} c_{11} & c_{12} & c_{13} & c_{14} & c_{15} & c_{16} \\ c_{21} & c_{22} & c_{23} & c_{24} & c_{25} & c_{26} \\ c_{31} & c_{32} & c_{33} & c_{34} & c_{35} & c_{36} \\ c_{41} & c_{42} & c_{43} & c_{44} & c_{45} & c_{46} \\ c_{51} & c_{52} & c_{53} & c_{54} & c_{55} & c_{56} \\ c_{61} & c_{62} & c_{63} & c_{64} & c_{65} & c_{66} \end{pmatrix} \begin{pmatrix} \varepsilon_{xx} \\ \varepsilon_{yy} \\ \varepsilon_{zz} \\ 2\varepsilon_{yz} \\ 2\varepsilon_{xz} \\ 2\varepsilon_{xy} \end{pmatrix}, \tag{2}$$

where $\mathbf{C}$ is the symmetrical elastic parameter matrix and $\boldsymbol{\varepsilon}$ is the strain vector. For a general anisotropic medium, there are 21 independent elastic coefficients in $\mathbf{C}$. The VTI medium is common in real-world scenarios, which contains five independent parameters c_{11}, c_{13}, c_{33}, c_{44}, and c_{66} with $c_{12} = c_{11} - 2c_{66}$. The elastic parameter matrix $\mathbf{C}$ in the VTI medium is:

$$\mathbf{C}_{\mathrm{VTI}} = \begin{pmatrix} c_{11} & c_{12} & c_{13} & 0 & 0 & 0 \\ c_{12} & c_{11} & c_{13} & 0 & 0 & 0 \\ c_{13} & c_{13} & c_{33} & 0 & 0 & 0 \\ 0 & 0 & 0 & c_{44} & 0 & 0 \\ 0 & 0 & 0 & 0 & c_{44} & 0 \\ 0 & 0 & 0 & 0 & 0 & c_{66} \end{pmatrix}. \tag{3}$$

In a 3D TI medium with Oxyz Cartesian coordinate system (see Fig. 1), the polarization angle θ is the angle between the symmetry axis and the z-axis, and the azimuth angle φ is the angle between the projection of the symmetry axis on the Oxy plane and the x-axis. Then, with the two angles θ and φ, the elastic parameter matrix $\mathbf{C}_{\mathrm{TI}}$ for a general TI medium can be obtained by (Wu et al., 2010; Kim et al., 2018):

$$\mathbf{C}_{\mathrm{TI}} = \mathbf{M}_{\varphi}\mathbf{M}_{\theta}\mathbf{C}_{\mathrm{VTI}}\mathbf{M}_{\theta}^{T}\mathbf{M}_{\varphi}^{T}, \tag{4}$$

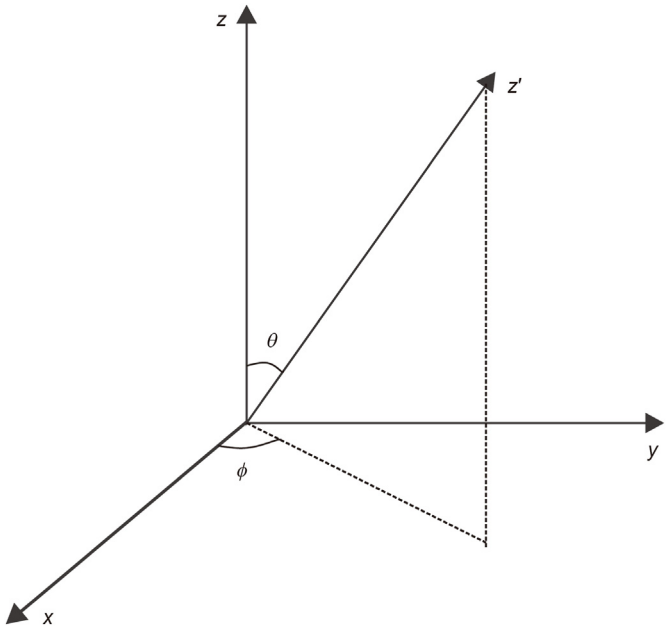

Fig. 1. Illustration of the symmetry axis and rotation angles, where θ and φ denote the polarization and azimuth angles, respectively.

where the transformation matrices $\mathbf{M}_\theta$ and $\mathbf{M}_\varphi$ are defined as:

$$\mathbf{M}_\theta = \begin{pmatrix} \cos^2\theta & 0 & \sin^2\theta & 0 & -\sin 2\theta & 0 \\ 0 & 1 & 0 & 0 & 0 & 0 \\ \sin^2\theta & 0 & \cos^2\theta & 0 & \sin 2\theta & 0 \\ 0 & 0 & 0 & \cos\theta & 0 & \sin\theta \\ \frac{\sin 2\theta}{2} & 0 & -\frac{\sin 2\theta}{2} & 0 & \cos 2\theta & 0 \\ 0 & 0 & 0 & -\sin\theta & 0 & \cos\theta \end{pmatrix}.$$

$$\mathbf{M}_\varphi = \begin{pmatrix} \cos^2\varphi & \sin^2\varphi & 0 & 0 & 0 & -\sin 2\varphi \\ \sin^2\varphi & \cos^2\varphi & 0 & 0 & 0 & \sin 2\varphi \\ 0 & 0 & 1 & 0 & 0 & 0 \\ 0 & 0 & 0 & \cos\varphi & \sin\varphi & 0 \\ 0 & 0 & 0 & -\sin\varphi & \cos\varphi & 0 \\ \frac{\sin 2\varphi}{2} & -\frac{\sin 2\varphi}{2} & 0 & 0 & 0 & \cos 2\varphi \end{pmatrix} \tag{6}$$

In 2D case, we assume that all the variables vary in the xz plane, then the partial derivatives with respect to y vanish. The source-free 2D three components form of Eq. (1) is given by:

$$\rho\frac{\partial}{\partial t}\begin{pmatrix} v_x \\ v_y \\ v_z \end{pmatrix} - \nabla\cdot\begin{pmatrix} \sigma_{xx} & \sigma_{xz} \\ \sigma_{xy} & \sigma_{yz} \\ \sigma_{xz} & \sigma_{zz} \end{pmatrix} = 0, \tag{6a}$$

and the stress equations varying with time are:

$$\frac{\partial}{\partial t}\begin{pmatrix} \sigma_{xx} \\ \sigma_{zz} \\ \sigma_{yz} \\ \sigma_{xz} \\ \sigma_{xy} \end{pmatrix} - \nabla\cdot\begin{pmatrix} c_{11}v_x + c_{16}v_y + c_{15}v_z & c_{15}v_x + c_{14}v_y + c_{13}v_z \\ c_{13}v_x + c_{36}v_y + c_{35}v_z & c_{35}v_x + c_{34}v_y + c_{33}v_z \\ c_{14}v_x + c_{46}v_y + c_{45}v_z & c_{45}v_x + c_{44}v_y + c_{34}v_z \\ c_{15}v_x + c_{56}v_y + c_{55}v_z & c_{55}v_x + c_{45}v_y + c_{35}v_z \\ c_{16}v_x + c_{66}v_y + c_{56}v_z & c_{56}v_x + c_{46}v_y + c_{36}v_z \end{pmatrix} = 0. \tag{7}$$

Here, $\nabla = (\partial_x, \partial_z)$ now is the 2D gradient operator. As can be seen, in such a case the P-SV and SH waves are coupled (Zhu and Dorman, 2000; Sun et al., 2016). For simplicity of presentations, we define $\mathbf{W} = (\sigma_{xx}, \sigma_{zz}, \sigma_{yz}, \sigma_{xz}, \sigma_{xy}, v_x, v_y, v_z)^T$ and introduce the following notations:

$$\mathbf{A}_1 = \begin{pmatrix} 0 & 0 & 0 & 0 & 0 & c_{11} & c_{16} & c_{15} \\ 0 & 0 & 0 & 0 & 0 & c_{13} & c_{36} & c_{35} \\ 0 & 0 & 0 & 0 & 0 & c_{14} & c_{46} & c_{45} \\ 0 & 0 & 0 & 0 & 0 & c_{15} & c_{56} & c_{55} \\ 0 & 0 & 0 & 0 & 0 & c_{16} & c_{66} & c_{56} \\ 1/\rho & 0 & 0 & 0 & 0 & 0 & 0 & 0 \\ 0 & 0 & 0 & 0 & 1/\rho & 0 & 0 & 0 \\ 0 & 0 & 0 & 1/\rho & 0 & 0 & 0 & 0 \end{pmatrix}, \mathbf{A}_2 = \begin{pmatrix} 0 & 0 & 0 & 0 & 0 & c_{15} & c_{14} & c_{13} \\ 0 & 0 & 0 & 0 & 0 & c_{35} & c_{34} & c_{33} \\ 0 & 0 & 0 & 0 & 0 & c_{45} & c_{44} & c_{34} \\ 0 & 0 & 0 & 0 & 0 & c_{55} & c_{45} & c_{35} \\ 0 & 0 & 0 & 0 & 0 & c_{56} & c_{46} & c_{36} \\ 0 & 0 & 0 & 1/\rho & 0 & 0 & 0 & 0 \\ 0 & 0 & 1/\rho & 0 & 0 & 0 & 0 & 0 \\ 0 & 1/\rho & 0 & 0 & 0 & 0 & 0 & 0 \end{pmatrix}, \tag{8}$$

then Eqs. (6) and (7) have a concise and compact form:

$$\frac{\partial \mathbf{W}}{\partial t} - \nabla\cdot(\mathbf{A}_1\mathbf{W}, \mathbf{A}_2\mathbf{W}) = \mathbf{0}, \tag{9}$$

where the item $(\mathbf{A}_1\mathbf{W}, \mathbf{A}_2\mathbf{W})$ is called the flux.

For a 2D VTI medium, the stress equations varying with time can be decoupled:

$$\begin{aligned} &\frac{\partial}{\partial t}\begin{pmatrix} \sigma_{xx} \\ \sigma_{zz} \\ \sigma_{xz} \end{pmatrix} - \nabla\cdot\begin{pmatrix} c_{11}v_x & c_{13}v_z \\ c_{13}v_x & c_{33}v_z \\ c_{55}v_z & c_{55}v_x \end{pmatrix} = 0\ , \\ &\frac{\partial}{\partial t}\begin{pmatrix} \sigma_{yz} \\ \sigma_{xy} \end{pmatrix} - \nabla\cdot\begin{pmatrix} 0 & c_{44}v_y \\ c_{66}v_y & 0 \end{pmatrix} = 0. \end{aligned} \tag{10}$$

Then, according, we have the following two equations:

$$\begin{aligned} &\rho\frac{\partial}{\partial t}\begin{pmatrix} v_x \\ v_z \end{pmatrix} - \nabla\cdot\begin{pmatrix} \sigma_{xx} & \sigma_{xz} \\ \sigma_{xz} & \sigma_{zz} \end{pmatrix} = 0, \\ &\frac{\partial}{\partial t}\begin{pmatrix} \sigma_{xx} \\ \sigma_{zz} \\ \sigma_{xz} \end{pmatrix} - \nabla\cdot\begin{pmatrix} c_{11}v_x & c_{13}v_z \\ c_{13}v_x & c_{33}v_z \\ c_{55}v_z & c_{55}v_x \end{pmatrix} = 0, \end{aligned} \tag{11}$$

and

$$\rho\frac{\partial}{\partial t}(v_y) - \nabla\cdot\begin{pmatrix} \sigma_{xy} & \sigma_{yz} \end{pmatrix} = 0, \frac{\partial}{\partial t}\begin{pmatrix} \sigma_{yz} \\ \sigma_{xy} \end{pmatrix} - \nabla\cdot\begin{pmatrix} 0 & c_{44}v_y \\ c_{66}v_y & 0 \end{pmatrix} = 0, \tag{12}$$

for the P-SV and SH waves, respectively. For the VTI media, an equation system similar to Eq. (9) can be obtained. The detail is not shown here to avoid lengthy descriptions.

3. Numerical scheme

3.1. Spatial discretization

We consider a domain $\Omega \in \mathbb{R}^2$, which is discretized into conforming elements with $\Omega = \bigcup_i \Omega_i$. Next, we define a scalar test function space:

$$V_h = \left\{\varphi \in L^2(\Omega) : \varphi|_{\Omega_i} \in P^\kappa(\Omega_i), \forall i\right\}, \tag{13}$$

where P^κ denotes the polynomial space at most κ-th order. Multiplying both sides of Eq. (9) by a scalar test function $\varphi(x,z)$ and integrating over Ω_i, we have:

$$\int_{\Omega_i}\left(\varphi\frac{\partial \mathbf{W}}{\partial t}-\varphi\nabla\cdot(\mathbf{A}_1\mathbf{W},\mathbf{A}_2\mathbf{W})\right)\mathrm{d}V=0. \tag{14}$$

Using the divergence theorem, we obtain:

$$\int_{\Omega_i}\left(\varphi\frac{\partial \mathbf{W}}{\partial t}+(\mathbf{A}_1\mathbf{W},\mathbf{A}_2\mathbf{W})\cdot\nabla\varphi\right)\mathrm{d}V-\int_{\partial\Omega_i}\varphi(\mathbf{A}_1\mathbf{W},\mathbf{A}_2\mathbf{W})\cdot\mathbf{n}\ \ \mathrm{d}S=0, \tag{15}$$

where $\mathbf{n}=(n_1,n_2)^T$ is the normal vector. In the DG framework, $\mathbf{W}$ is allowed to be discontinuous at $\partial\Omega_i$, so the item $(\mathbf{A}_1\mathbf{W},\mathbf{A}_2\mathbf{W})\cdot\mathbf{n}$ should be modified and replaced by the numerical flux. We use the local Lax-Friedrichs numerical flux, which replaces $(\mathbf{A}_1\mathbf{W},\mathbf{A}_2\mathbf{W})\cdot\mathbf{n}$ by $\widehat{\mathbf{A}}^{\mathrm{int}}\mathbf{W}^{\mathrm{int}}+\widehat{\mathbf{A}}^{\mathrm{ext}}\mathbf{W}^{\mathrm{ext}}$, where $\mathbf{W}^{\mathrm{int}}$ and $\mathbf{W}^{\mathrm{ext}}$ the traces of $\mathbf{W}$ on $\partial\Omega_i$, and

$$\begin{aligned}\widehat{\mathbf{A}}^{\mathrm{int}}&=\frac{1}{2}(\mathbf{A}_1n_1+\mathbf{A}_2n_2+\upsilon_{\partial\Omega_i}\mathbf{I}),\\ \widehat{\mathbf{A}}^{\mathrm{ext}}&=\frac{1}{2}(\mathbf{A}_1n_1+\mathbf{A}_2n_2-\upsilon_{\partial\Omega_i}\mathbf{I}).\end{aligned} \tag{16}$$

Here, $\mathbf{I}$ is the identity matrix, and $\upsilon_{\partial\Omega_i}$ is a parameter called the numerical viscosity which can be evaluated as the largest speed on $\partial\Omega_i$.

To load the free surface boundary condition, we can take an exterior velocity wavefield that is identical to the interior wavefield, and impose an opposite stress wavefield. As a result, we can keep a continuous velocity and a zero stress on the free surface (Etienne et al., 2010). To load the absorbing boundary condition (ABC), we let $\widehat{\mathbf{A}}^{\mathrm{ext}}\mathbf{W}^{\mathrm{ext}}=0$. Mathematically, it means that the external waves are not allowed to enter the domain. It is worth noting that this is the simplest way to deal with the ABCs, but the absorption effect of this treatment is not very good, as will be seen later in the modeling example.

We now turn to the basis expansion of $\mathbf{W}$. First, we express $\mathbf{W}$ as:

$$\mathbf{W}\ |_{\Omega_i}=\sum_{l=1}^{N}\mathbf{C}_l^i(t)\varphi_l^i, \tag{17}$$

where $\{\varphi_l^i\}_{l=1}^N$ are the time-independent basis functions, $\{\mathbf{C}_l^i(t)\}_{l=1}^N$ are the coefficients of the unknowns, and N is the number of basis functions. There are many options for the choice of $\{\varphi_l^i\}_{l=1}^N$ (de Basabe et al., 2008; de la Puente, 2008). Numerical tests show that all commonly used basis functions are applicable. We then combine Eqs. (15)–(17) to obtain the following semi-discrete scheme:

in which Ω_j is the adjacent element of Ω_i.

3.2. Time discretization

After the DG spatial discretization, we obtain the semi-discrete scheme in Eq. (18), which is now an ordinary differential system. For simplicity of notations, we use a vector $\mathbf{C}(t)$ to denote all the coefficients, and use a linear operator L to denote the DG formulations of spatial discretization, then Eq. (18) can be expressed as:

$$\frac{\partial \mathbf{C}}{\partial t}=L(\mathbf{C}). \tag{19}$$

Here, we use a weighted explicit Runge-Kutta method to solve Eq. (19) (He et al., 2015), which says:

$$\mathbf{C}^{(n+1)}=\mathbf{C}^{(n)}+\frac{\Delta t}{2}\left(\mathbf{K}^{(n)}+\overline{\mathbf{K}}^{(n)}\right), \tag{20}$$

where $\mathbf{K}^{(n)}$ and $\overline{\mathbf{K}}^{(n)}$ are two intermediate variables, which are evaluated using the following two equations:

$$\begin{cases}\mathbf{K}_0^{(n)}=L\left(\mathbf{C}^{(n)}\right)\\ \mathbf{K}_1^{(n)}=r\Delta tL\left(\mathbf{K}_0^{(n)}\right)+L\left(\mathbf{C}^{(n)}\right)\\ \mathbf{K}_2^{(n)}=r\Delta tL\left(\mathbf{K}_1^{(n)}\right)+L\left(\mathbf{C}^{(n)}\right)\\ \mathbf{K}^{(n)}=\eta\mathbf{K}_2^{(n)}+(1-\eta)\mathbf{K}_1^{(n)}\end{cases}, \tag{21}$$

and

$$\begin{cases}\mathbf{T}^{(n)}=\mathbf{C}^{(n)}+(1-2r)\Delta t\mathbf{K}^{(n)}\\ \overline{\mathbf{K}}_0^{(n)}=L\left(\mathbf{T}^{(n)}\right)\\ \overline{\mathbf{K}}_1^{(n)}=r\Delta tL\left(\overline{\mathbf{K}}_0^{(n)}\right)+L\left(\mathbf{T}^{(n)}\right)\\ \overline{\mathbf{K}}_2^{(n)}=r\Delta tL\left(\overline{\mathbf{K}}_1^{(n)}\right)+L\left(\mathbf{T}^{(n)}\right)\\ \overline{\mathbf{K}}^{(n)}=\eta\overline{\mathbf{K}}_2^{(n)}+(1-\eta)\overline{\mathbf{K}}_1^{(n)}\end{cases}, \tag{22}$$

where $r=(3-\sqrt{3})/6$, and $\eta\in[0,1]$ is a weighting factor.

It should be noted that some time-stepping scheme cannot obtain stable full-discrete numerical schemes when combining with DG space discretization formulations. For example, He et al. (2019a) studied the stability conditions for the arbitrary high-order derivative (ADER) time-stepping method (Käser and Dumbser, 2006; de la Puente et al., 2007) and the weighted Runge-Kutta method. They found that the ADER time-stepping method with the centred flux DG formulation is unstable, but the weighted Runge-Kutta method is stable and robust that matches

$$\sum_{l=1}^{N}\frac{\partial \mathbf{C}_l^i(t)}{\partial t}\iint_{\Omega_i}\varphi_l^i\varphi_{l'}^i\,\mathrm{d}V-\sum_{l=1}^{N}\mathbf{A}_1\mathbf{C}_l^i(t)\iint_{\Omega_i}\varphi_l^i\frac{\partial\varphi_{l'}^i}{\partial x}\mathrm{d}V-\sum_{l=1}^{N}\mathbf{A}_2\mathbf{C}_l^i(t)\iint_{\Omega_i}\varphi_l^i\frac{\partial\varphi_{l'}^i}{\partial z}\mathrm{d}V+\sum_{l=1}^{N}\sum_j\widehat{\mathbf{A}}^{\mathrm{int}}\mathbf{C}_l^i(t)\int_{\Omega_i\cap\Omega_j}\varphi_l^i\varphi_{l'}^i\,\mathrm{d}l+\sum_{l=1}^{N}\sum_j\widehat{\mathbf{A}}^{\mathrm{ext}}\mathbf{C}_l^j(t)\int_{\Omega_i\cap\Omega_j}\varphi_l^j\varphi_{l'}^i\,\mathrm{d}l=0,$$

$$l'=1,\ldots,N;\forall i \tag{18}$$

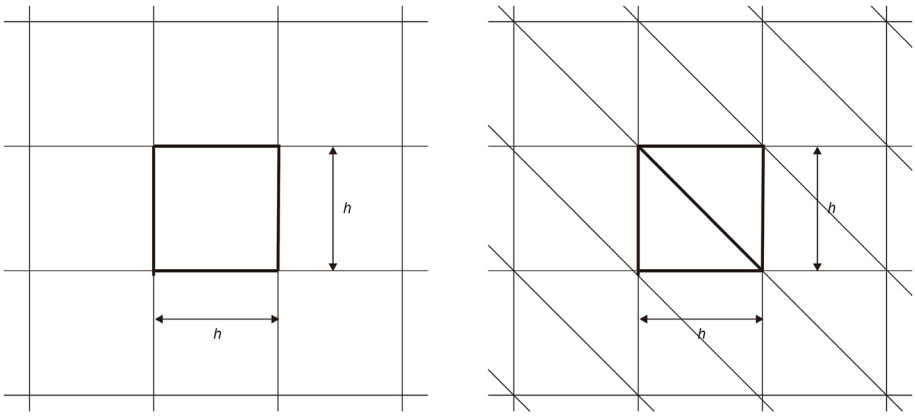

Fig. 2. Rectangular and triangular elements (He et al., 2019a).

Table 1
The CFL condition numbers for the weighted RKDG method.

	η	0.0	0.1	0.2	0.3	0.4	0.5	0.6	0.7	0.8	0.9	1.0
P^1	rec	0.592	0.668	0.818	1.04	0.982	0.784	0.676	0.61	0.562	0.528	0.5
	tri	0.344	0.388	0.476	0.575	0.570	0.456	0.393	0.354	0.326	0.306	0.290
P^2	rec	0.224	0.232	0.242	0.254	0.27	0.292	0.324	0.32	0.294	0.276	0.262
	tri	0.139	0.145	0.151	0.159	0.169	0.182	0.203	0.194	0.179	0.168	0.159

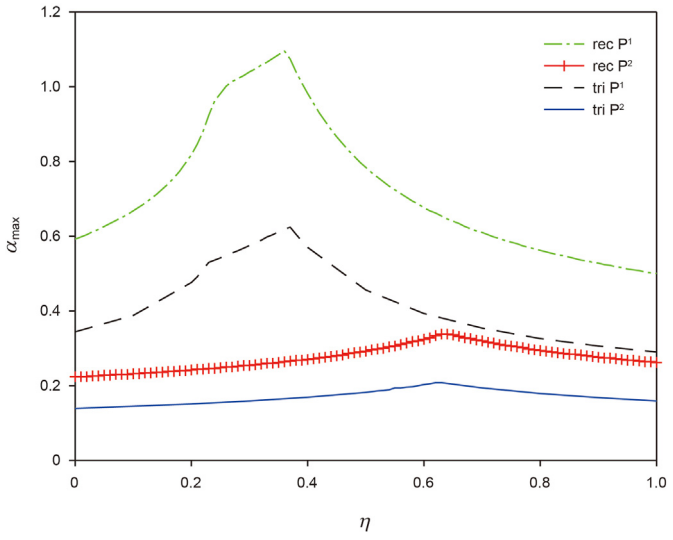

Fig. 3. The CFL condition numbers of the weighted RKDG method for η varying from 0 to 1.

well with most DG methods. He et al. (2019a) also showed that the weighted Runge-Kutta method introduced smaller numerical dispersion than the popular ADER time-stepping method. Moreover, the weighted Runge-Kutta method introduces a weighting factor, which allows the stability condition number to be optimized. We can choose the optimal weighting factor to maximize the stability condition number.

4. Stability

Next, we derive the numerical stability conditions for the weighted RKDG method to solve the elastic equations in anisotropic media. We use the Courant-Friedrichs-Lewy (CFL) condition number α_{max}, to constrain the selections of the spatial step h, the time step Δt, and the wave speed c. These parameters need to satisfy the following inequality: $\Delta t \leq \alpha_{max}\frac{h}{c}$, in which α_{max} is also called the maximum Courant number. Here, we do not intend to perform a detailed and lengthy stability analysis of the anisotropic media, but instead we use the results of existing studies conducted by He et al. (2015, 2019a), in which they provided the stability conditions of the scalar wave equation for the uniform rectangular and triangular meshes (shown in Fig. 2). In Table 1, we list the values of α_{max} for the two meshes with η between 0 and 1 at an interval of 0.1. We see from Table 1 that as the weighting coefficient η changes from 0 to 1, α_{max} tends to increase first and then decrease. We also plot the maximal Courant numbers for the weighting factor η in Fig. 3. More detailed calculation for a finer sampling of η (at an interval of 0.01) shows: for the P^1 case with a rectangular mesh, $\eta = 1$ gives the smallest α_{max} with $\alpha_{max} \approx 0.5$, and $\eta = 0.36$ gives the largest α_{max} with $\alpha_{max} \approx 1.096$. For the P^1 case with a triangular mesh, $\eta = 1$ gives the smallest α_{max} with $\alpha_{max} \approx 0.290$, and $\eta = 0.37$ gives the largest α_{max} with $\alpha_{max} \approx 0.624$. For the P^2 case with a rectangular mesh, $\eta = 0$ gives the smallest α_{max} with $\alpha_{max} \approx 0.224$, and $\eta = 0.63$ gives the largest α_{max} with $\alpha_{max} \approx 0.338$. For the P^2 case with a triangular mesh, $\eta = 0$ gives the smallest α_{max} with $\alpha_{max} \approx 0.139$, and $\eta = 0.63$ gives the largest α_{max} with $\alpha_{max} \approx 0.208$. Then, to obtain a larger time step, for the P^1 case with rectangular mesh, we can use $\eta = 0.36$; for the P^1 case with triangular mesh, we can use $\eta = 0.37$; for the P^2 case with rectangular and triangular meshes, we use $\eta = 0.63$.

In the above stability conditions for the triangular mesh, the side length h of the triangle in Fig. 2b is used. If we use the diameter d of the inscribed circle in the triangle in Fig. 2b, then the time step needs to satisfy the following condition:

$$\Delta t \leq \alpha'_{max} \min\left(\frac{h}{c}\right) \approx \left(\frac{1+\cot(\pi/8)}{2}\right)\alpha_{max} \min\left(\frac{d}{c}\right). \tag{23}$$

In actual numerical calculations, we find that Eq. (23) is a good estimate for the time step.

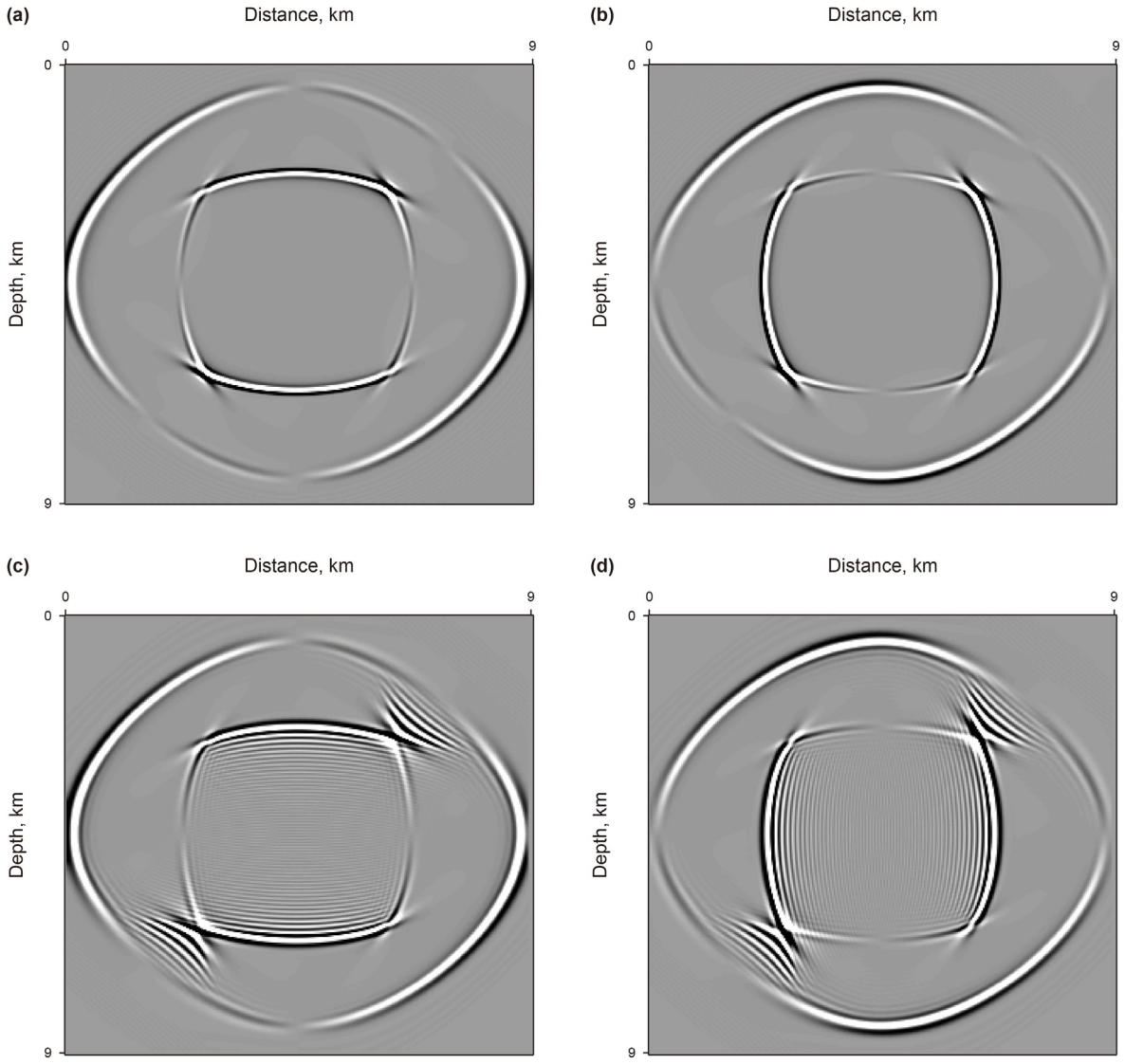

Fig. 4. Wavefield snapshots at $T = 0.7$ s in the VTI model. (a) and (b) show the v_x and v_z wavefields obtained using the weighted RKDG method; (c) and (d) show the v_x and v_z wavefields obtained using the SG method. The 30 m × 30 m rectangular mesh is used.

The above results are applicable to the acoustic equation. In fact, we can directly use Eq. (23) to obtain an effective stability condition appropriate for anisotropic media. We just need to replace the acoustic wave velocity in Eq. (23) with the maximum velocity in all directions in the anisotropic media. Numerical experiments show that this treatment works well, but we have no theoretical proof.

5. Modeling examples

We now present some numerical modeling tests to demonstrate the effectiveness of the weighted RKDG method for solving elastic wave equations in anisotropic media. Before proceeding further, we remark that high-order DG methods (P^κ, $\kappa > 2$) have small CFL condition numbers and expensive computing costs, so, here we use the P^2 weighted RKDG method.

5.1. Homogeneous VTI model

The first example simulates the P-SV wave propagation in a homogeneous VTI medium. The elastic parameters are $c_{11} = 44.8$ GPa, $c_{13} = 9.5$ GPa, $c_{33} = 37.6$ GPa, and $c_{55} = 11.8$ GPa. We set the density $\rho = 1.0$ g/cm^3. The computational domain is a square with side length of 9 km. We set the source at (4.5 km, 4.5 km) with the source function:

$$f(t) = \Big(1 - 2(\pi f_0(t - t_0))^2\Big) \exp\Big(-(\pi f_0(t - t_0))^2\Big), \tag{24}$$

in which t_0 denotes the delay time with $t_0 = 1/f_0$ and $f_0 = 20$ Hz. The 30 m × 30 m rectangular mesh is used. We carry out the simulation using the weighted RKDG method with a weighting factor $\eta = 0.63$ to allow for the maximum stable time step $\alpha_{\max} \approx 0.338$. The maximum velocity in the anisotropic medium is $c = 6.693$ km/s. Then, according to Eq. (23), we have $\Delta t \approx 1.512$ ms.

Fig. 4 presents the snapshots at $T = 0.7$ s. We compare our modeling results with those generated by the fourth-order staggered grid (SG) method (Virieux, 1986) using the same parameters. The anisotropy of wave propagation is clearly seen in Fig. 4a and b. However, there is serious numerical dispersion for the SG method in Fig. 4c and d. If the SG method achieves the same effect as our method, a finer mesh (7.5 m × 7.5 m) is needed. In this case, these

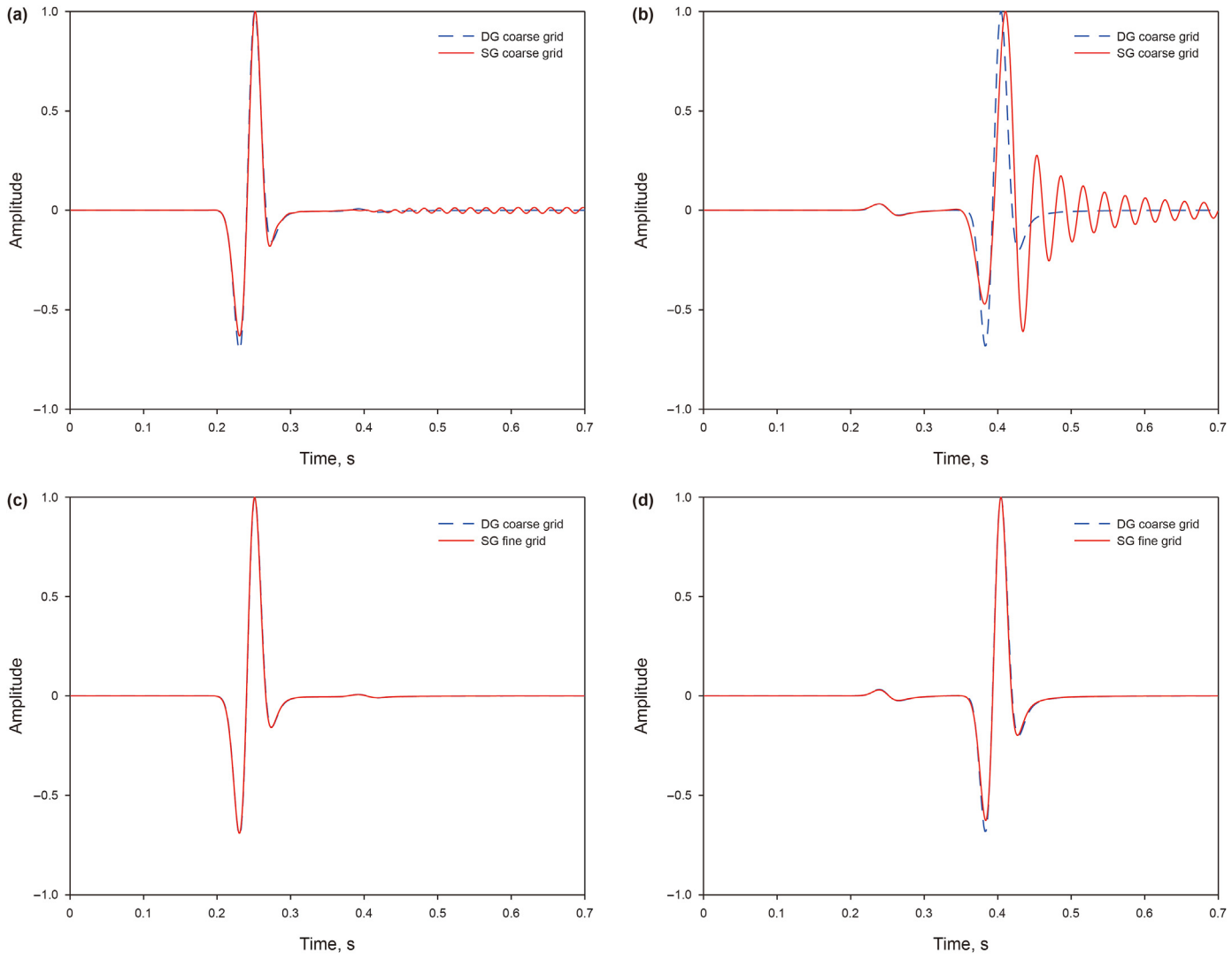

Fig. 5. Synthetic waveforms at $T = 0.7$ s for the VTI model. (a) v_x and (b) v_z are obtained using the two methods on the same coarse mesh (30 m × 30 m), whereas (c) v_x and (d) v_z are obtained using the weighted RKDG method on coarse mesh (30 m × 30 m) and the SG method on fine mesh (7.5 m × 7.5 m).

two methods produce the similar snapshots of the seismic waves without visible numerical dispersion. We also set a receiver at (4.5 km, 5.7 km) to record the waveforms. Fig. 5 presents the synthetic waveforms of the two methods. Overall, we see that the weighted RKDG solutions on coarse mesh match the SG solutions on fine mesh, validating the correctness and effectiveness of our method.

Next, we compare the calculation and storage of the two methods. We carry out the simulations on the same personal computer. It takes 9955 s for the weighted RKDG method to finish the simulation on coarse grid, whereas it takes only 788 s for the SG method on fine grid. We see that the DG method is computationally expensive, compared with FDM. Considering the storage, the weighted RKDG method takes up approximately 16.5 Mb, and the SG method takes up nearly 132 Mb. The reason for the small storage of the DG method is that it uses coarse grids but produces small numerical dispersion. Combined with the non-uniform unstructured mesh techniques (e.g., coarse mesh for high velocity areas and fine mesh for low velocity areas), the DG method can significantly reduce the size of the problem, thereby reducing the amount of memory and computation. However, the conventional FDM can only use a uniform fine mesh for the non-uniform velocity model, which leads to a large amount of storage and calculation.

To test the effect of our ABC combined with the weighted RKDG method, we extend the simulation time to $T = 0.9$ s and 1.1 s. Fig. 6 shows the wavefield snapshots, from which we observe that the P wave has propagated to the boundary and is reflected. It is seen from the figure that our ABC can absorb most of the wave energy reflected by the boundary, but as shown by the arrow in the figure, we still observe the existence of some weaker reflected waves. This example shows that our ABC has a certain absorbing effect, but the effect is not perfect. We will try other kinds of ABCs in the future, such as perfectly matched layers.

5.2. TTI model with titled slope

In this example we consider a 2D Lamb problem (Lamb, 1904). The physical domain stretches 4 km in the x axis, and the depth of the left boundary is 2 km in the z axis with a slope of a tilt angle $\theta = 10^o$. Here, we choose the elastic material parameters as: $\rho = 2.1$ g/cm^3, $c_{11} = 25.2$ GPa, $c_{12} = 12.0$ GPa, $c_{13} = 6.0$ GPa, $c_{33} = 15.0$ GPa, $c_{44} = 4.38$ GPa, and $c_{66} = 6.6$ GPa. The corresponding TTI model is obtained by tilting the symmetry axis of the VTI by $\theta = 10^o$. We divide the entire computational area into 23864

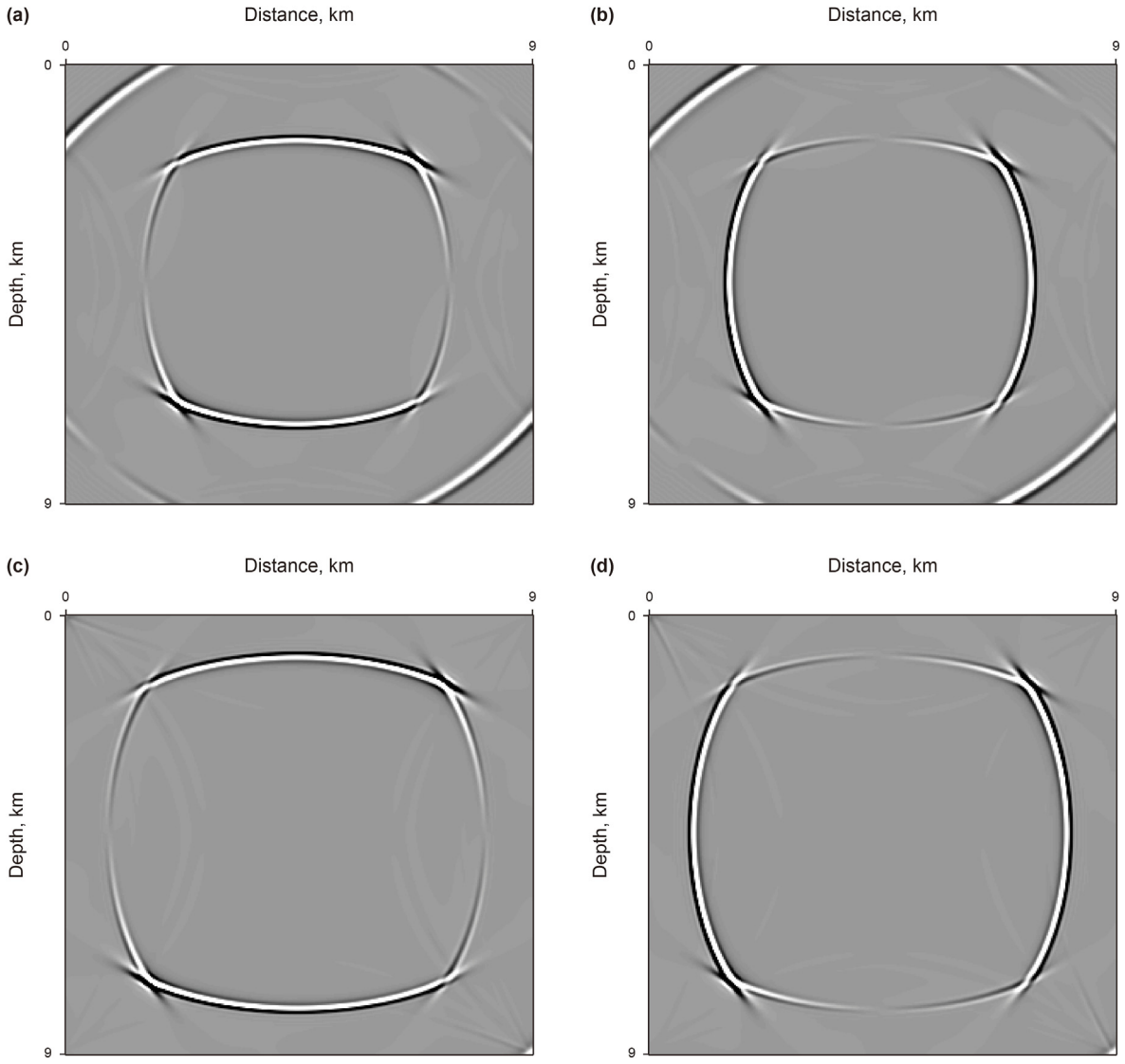

Fig. 6. Wavefield snapshots at $T = 0.9$ s and 1.1 s in the VTI model. (a) and (b) show v_x and v_z wavefields at $T = 0.9$ s; (c) and (d) show v_x and v_z wavefields at $T = 1.1$ s. The areas pointed by the arrow indicate that there are still some reflections from the boundary.

triangles, and the diameter of the smallest inscribed circle is $d \approx 14$ m. According to the elastic parameters in this experiment, the maximum wave speed in the anisotropic medium is $c = 3.464$ km/s. We carry out the simulation using the weighted RKDG method with $\eta = 0.5$. In this case $\alpha_{\max} \approx 0.182$. Then, according to Eq. (23), we have $\Delta t \approx 1.265$ ms. We set a Ricker wavelet source on the surface of the slope, and the location coordinates are (1.720 km, 2.303 km) with frequency $f_0 = 12$ Hz.

Fig. 7 presents the snapshots of the three-components of the velocity fields in the TTI medium at times $T = 0.35$ s and 0.55 s. From the snapshots we can clarify the anisotropic features of the propagation. For v_x (panels a and b) and v_z (panels e and f) components, we see that the P-SV waves is decoupled from the SH wave. The transverse symmetry axis has an inclination of 10^o relative to the horizontal plane, just parallel to the slope. Fig. 7c and d shows the v_y components, from which the anisotropy and tilt features are also very clear. The snapshots in the figure have no visible numerical dispersion, demonstrating that our method can handle wave propagation in TTI media correctly.

5.3. VTI and TTI models with surface topography

In this example, we investigate elastic wavefields in VTI and TTI media with surface topography. The model is a Gaussian hill (we note that this model has been used by He et al., [2020b] to study the acoustic wave propagation). We discretize the physical domain by 31901 triangles, and the diameter of the smallest inscribed circle is $d \approx 18.3$ m. We carry out the simulation using the weighted RKDG method with $\eta = 0.63$ to allow for the maximum stable time step $\alpha_{\max} \approx 0.208$. The time step is $\Delta t \approx 1.768$ ms. We use a Ricker wavelet source with peak frequency $f_0 = 12$ Hz, and its location coordinates are (3.6 km, 2.4 km). In the first case we consider a VTI medium with the elastic material parameters: $\rho = 3.0$ g/cm^3, $c_{11} = 40.5$ GPa, $c_{12} = 23.4$ GPa, $c_{13} = 12.8$ GPa, $c_{33} = 27.0$ GPa, $c_{44} = 6.75$ GPa, and $c_{66} = 8.55$ GPa. Then, we rotate the symmetry axis of the VTI medium and obtain two TTI media: case 1 with $\theta = 30^o$, $\varphi = 0^o$ and case 2 with $\theta = 30^o$, $\varphi = 45^o$. In case 2, the 21 elastic material parameters are non-zero.

Figs. 8 and 9 presents the snapshots at $T = 0.35$ s and 0.8 s,

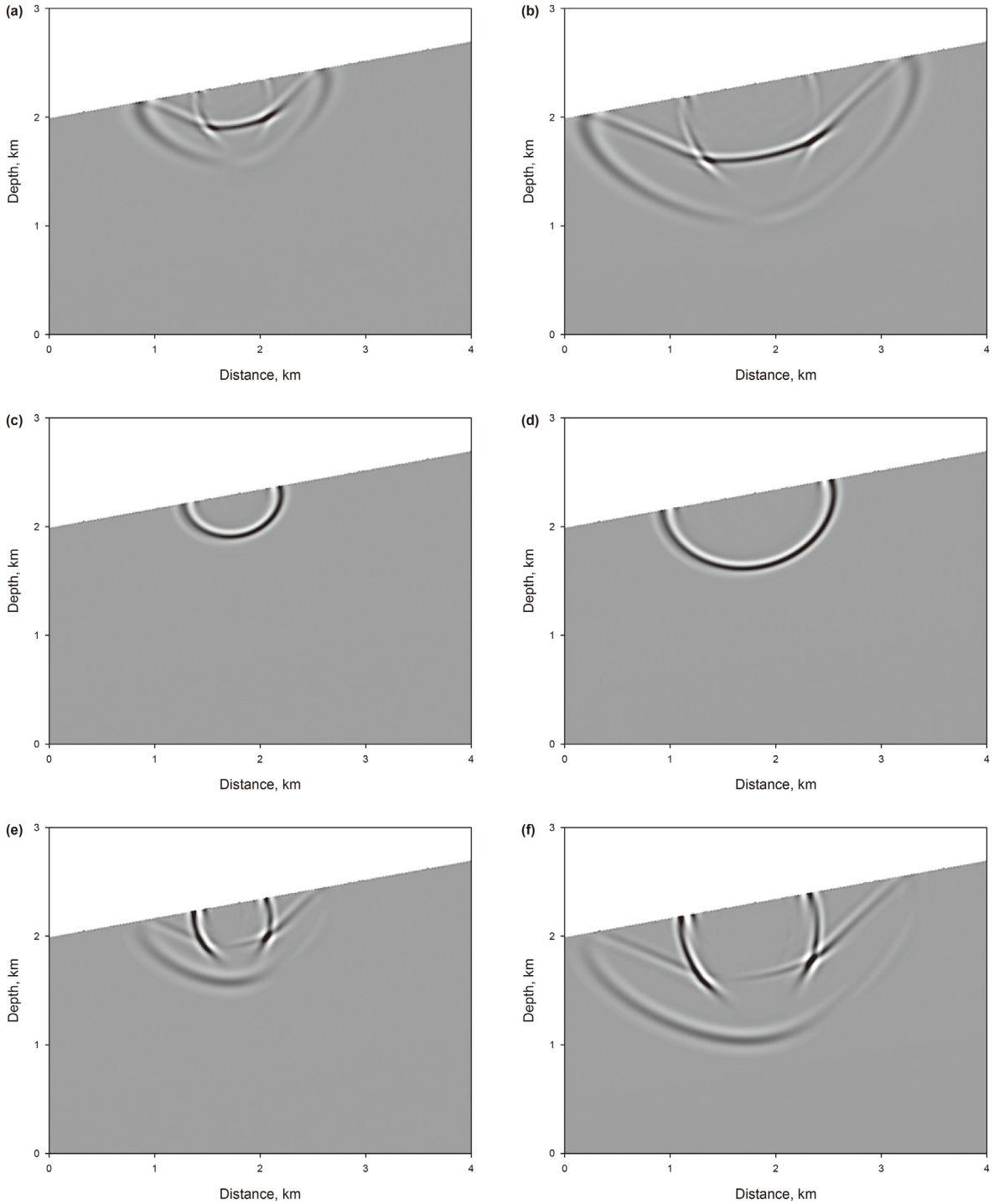

Fig. 7. Snapshots of the three-components velocity fields in the TTI medium at time $T = 0.35$ s (a, c and e) and $T = 0.55$ s (b, d and f). (a–b): v_x; (c–d): v_y; (e-f): v_z. Note that the symmetry axis has a $\theta = 10^o$ tilt angle.

respectively. From the two figures, we can see the obvious anisotropic features of wavefields. We see that the P-SV and SH wavefields are separated for VTI and TTI case 1. But, for the TTI medium in case 2, the P-SV and SH waves are coupled. The numerical results demonstrate that the weighted RKDG method can simulate wave propagation for the complicated TTI model with surface topography.

In addition, we compare the computation cost of our method for the three media - VTI, TTI case 1, and TTI case 2. On the same computing platform, the CPU times required to simulate the wave propagation to $T = 0.8$ s in the three media are 229 s, 236 s and 256 s, respectively. We see that TTI case 2 costs the longest time and VTI costs the shortest. This is reasonable because the elastic parameter matrix **C** (in Eq. (3)) of TTI case 2 is the densest with 36 non-zero entries, which introduces more partial derivatives and more computation. The elastic parameter matrix **C** of TTI case 1 has 20 non-zero entries, and VTI has 12 non-zero entries. We see that although the elastic matrix **C** in TTI case 2 and TTI case 1 are much

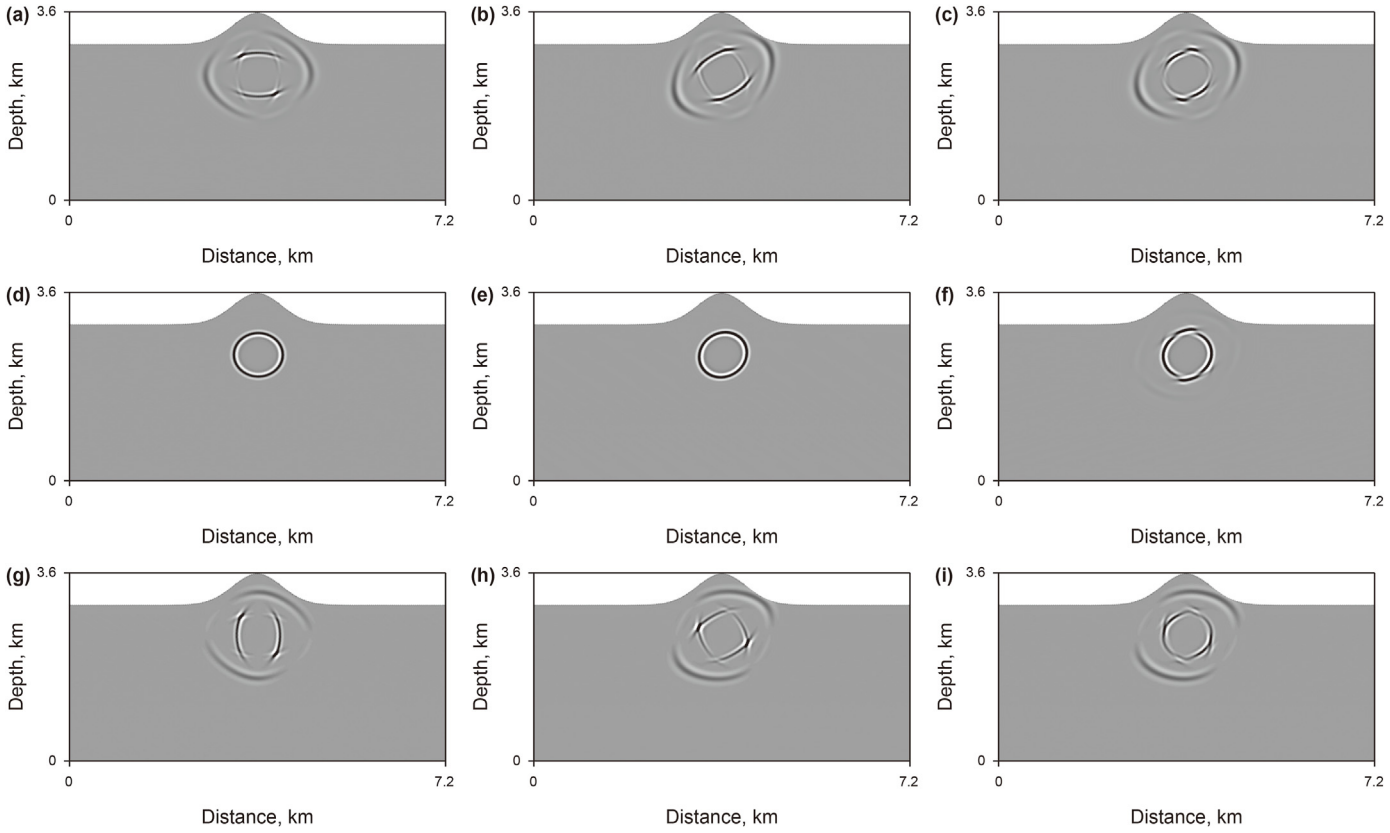

Fig. 8. Wavefield snapshots at $T = 0.35$ s for the VTI and TTI media. (a), (d) and (g): v_x; (b), (e) and (h): v_y; (c), (f) and (i): v_z. (a), (b) and (c) are for the VTI medium; (d), (e) and (f) are for the TTI medium with $\theta = 30^o$, $\varphi = 0^o$; (g), (h) and (i) are for the TTI medium with $\theta = 30^o$, $\varphi = 45^o$.

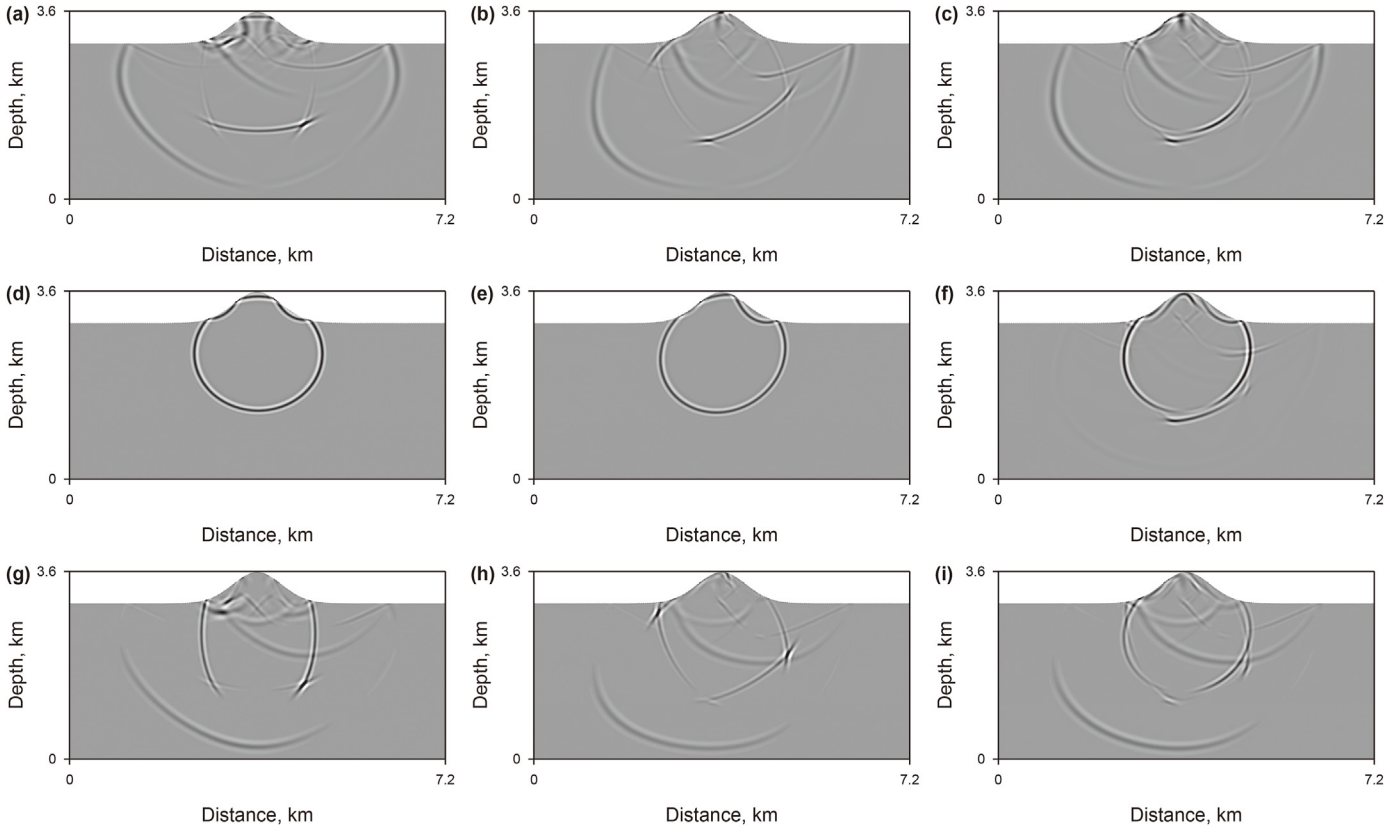

Fig. 9. Wavefield snapshots at $T = 0.8$ s for the VTI and TTI media. Panels are the same as in Fig. 8.

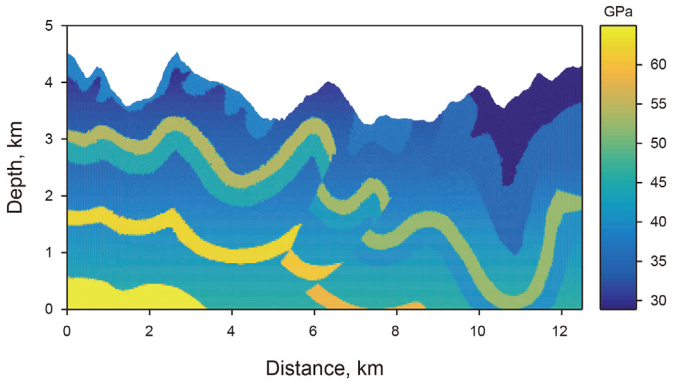

Fig. 10. The elastic parameter c_{11} of the heterogeneous Canadian foothills model.

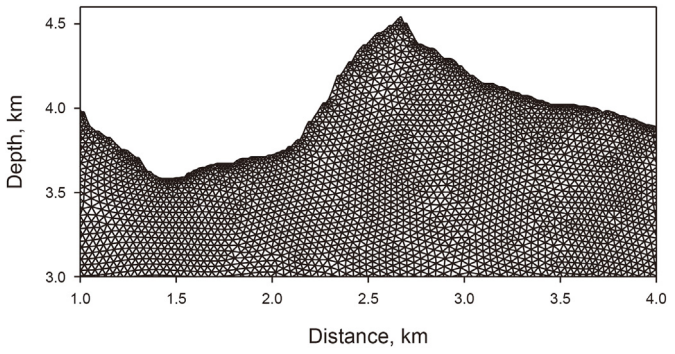

Fig. 11. Part of the mesh for the heterogeneous Canadian foothills model.

denser than VTI, the CPU times are only 12% and 3% more. This demonstrates that our method is computationally efficient for wave modeling in complex TTI media.

5.4. Heterogeneous canadian foothills model

In this example, the weighted RKDG method is applied to the seismic elastic wave simulations of rugged topographic surface in complex heterogeneous TTI medium. Here, we use a part of the classic Canadian foothills model, which belongs to the thrust fault structures in northeastern British Columbia, Canada, and is widely used to test the surface topography (Liu et al., 2017; Qiu et al., 2020; Shragge and Konuk, 2020). We choose a horizontal extension distance of 12.495 km and a vertical depth of 4.542 km. The surface has large undulations, with a maximum undulation depth of approximately 1.5 km. For this model, we use a TTI medium which is obtained by rotating the VTI medium with $\theta = 30^o$, $\varphi = 0^o$. The distribution of the elastic parameter c_{11} is shown in Fig. 10. We see that this model not only has heterogeneous layered structures inside, but also contains some faults. The speed varies from 3.8 km/s to 5.7 km/s. Other elastic parameters are set as follows: $\rho = 2.0$ g/cm^3, $c_{12} = 0.57c_{11}$, $c_{13} = 0.32c_{11}$, $c_{33} = 0.67c_{11}$, $c_{44} = 0.17c_{11}$, and $c_{66} = (c_{11} - c_{12})/2$.

Because the model has large fluctuations on the surface, we divided the domain with an irregular triangular mesh. A total of 86,414 triangular elements are used, and the number of vertices is 43,960. Fig. 11 shows the mesh division of a local area with large drop. We see a denser mesh near the surface than that in the subsurface. Since the elastic parameters of the original Canadian foothills model is defined on the equidistant rectangular grid points, here we use an interpolation method to convert the elastic parameters on the rectangular grid points into triangular elements.

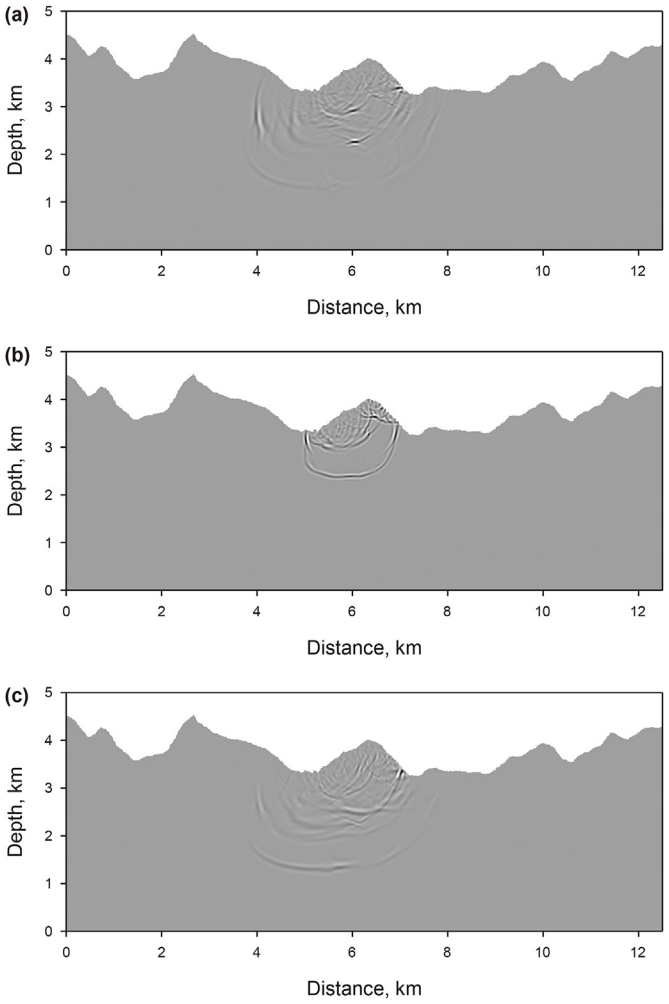

Fig. 12. Snapshots of the wavefields in the TTI medium for the Canadian foothills model at $T = 0.6$ s. (a), (b), and (c) show the v_x, v_y, and v_z components, respectively.

The side length of the triangular elements we used did not exceed 35 m. The minimum value of d/c in Eq. (23) is approximately 1.334×10^{-3}. We carry out the simulation using the weighted RKDG method with $\eta = 0.63$, then $\alpha_{\max} \approx 0.208$. According to Eq. (23), the time step is 4.737×10^{-4}. We use a Ricker wavelet source with peak frequency $f_0 = 20$ Hz, and its location coordinates are (6.0 km, 3.5 km). Free surface boundary conditions are used for the surface boundary of the model.

Figs. 12 and 13 exhibit the resulting wavefields at $T = 0.6$ s and 0.9 s, respectively. The two simulations lasted for 3072 s and 2049 s, respectively, in an Intel Xeon X5670 2.93 GHz processor. In the two figures, panel (a) shows the v_x component, panel (b) shows the v_y component, and panel (c) show the v_z component. The scattering of the wavefields due to the irregular surface topography can be clearly seen from the figure. The elastic wavefield energy varies due to the internal heterogeneous velocity structures, with energy being enhanced in some areas and weakened in other areas. This example shows that the weighted RKDG method is capable of simulating wavefields in complex heterogeneous anisotropic media with surface topography.

6. Conclusions and discussions

We develop a weighted RKDG approach for simulate elastic wavefields in 2D TI media. Both VTI and TTI media are considered.

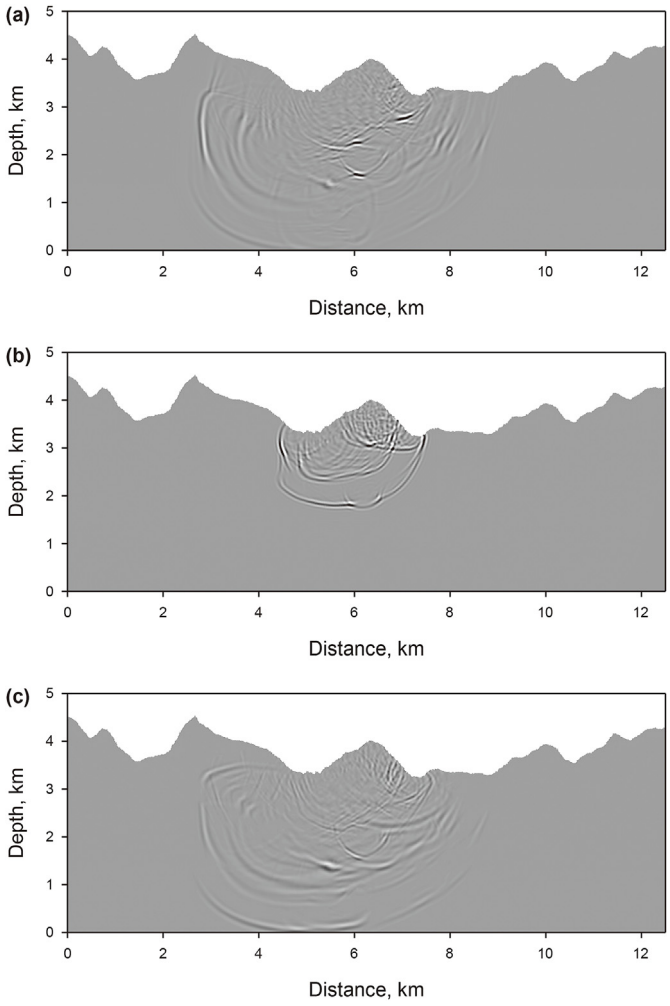

Fig. 13. Snapshots of the wavefields in the TTI medium for the Canadian foothills model at $T = 0.9$ s. (a), (b), and (c) show the v_x, v_y, and v_z components, respectively.

This method is also applicable to all general anisotropic media. The unstructured triangular meshes in 2D case are used for simulations. The effectiveness of this method is demonstrated by several numerical examples in homogeneous and heterogeneous media with regular and irregular geometries. We also compare the numerical results of our method with the classic SG method in the homogeneous VTI model. It is shown that our method can reduce the numerical dispersion on coarse grids with higher computational cost and smaller memory storage compared to the classical SG method. Moreover, we believe that the weighted RKDG method is promising for wave simulation in various complex heterogeneous anisotropic media by using non-uniform meshes, that is, in the low velocity region we can use a dense mesh, and in the high velocity region we can use a coarse mesh. Then, we can avoid using dense meshes in all regions, which will greatly reduce the number of meshes and increase the time step. Therefore, the weighted RKDG method can improve the computational efficiency of the simulations in heterogeneous anisotropic media. Furthermore, since high-performance computing can significantly improve the computing efficiency, we will parallelize our method to solve the wave propagation problems in TI media in future research.

Statements and declarations

The authors declare that they have no known competing financial interests or personal relationships that could have appeared to influence the work reported in this paper.

Acknowledgments

The authors thank the editors and three anonymous reviewers for their detailed comments and helpful suggestions that greatly contributed to improving the manuscript. This work was supported by the National Natural Science Foundation of China (Grant Nos. 41974114, 41604105) and the Fundamental Research Funds for the Central Universities (2020YQLX01). The work of Xijun He was also supported in part by the Project of Cultivation for Young Top-notch Talents of Beijing Municipal Institutions under Grant BPHR202203047 and in part by the Young Elite Scientists Sponsorship Program by BAST.

References

Aki, K., Richards, P.G., 2002. Quantitative Seismology. University Science Books, California.

Carcione, J.M., 2007. Wave Fields in Real Media: Wave Propagation in Anisotropic, Anelastic, Porous and Electromagnetic Media. Elsevier, Oxford.

Carcione, J.M., Santos, J.E., Picotti, S., 2011. Anisotropic poroelasticity and wave-induced fluid flow: harmonic finite-element simulations. Geophys. J. Int. 186, 1245–1254. https://doi.org/10.1088/1751-8113/46/34/345501.

Clare, M.C., Percival, J.R., Angeloudis, A., Cotter, C.J., Piggott, M.D., 2020. Hydro-morphodynamics 2D modelling using a discontinuous Galerkin discretization. Comput. Geosci. 146, 104658. https://doi.org/10.1016/j.cageo.2020.104658.

Cockburn, B., Shu, C.W., 1989. TVB Runge-Kutta local projection discontinuous Galerkin finite element method for conservation laws II: general framework. Math. Comput. 52, 411–435. https://doi.org/10.1090/S0025-5718-1989-0983311-4.

Cockburn, B., Shu, C.W., 2001. Runge–Kutta discontinuous Galerkin methods for convection- dominated problems. J. Sci. Comput. 16, 173–261. https://doi.org/10.1023/A:1012873910884.

de Basabe, J.D., Sen, M.K., Wheeler, M.F., 2008. The interior penalty discontinuous Galerkin method for elastic wave propagation: grid dispersion. Geophys. J. Int. 175, 83–93. https://doi.org/10.1111/j.1365-246X.2008.03915.x.

de Basabe, J.D., Sen, M.K., Wheeler, M.F., 2016. Elastic wave propagation in fractured media using the discontinuous Galerkin method. Geophysics 81, T163–T174. https://doi.org/10.1190/geo2015-0602.1.

de la Puente, J., 2008. Seismic Wave Simulation for Complex Rheologies on Unstructured Meshes. Ludwig-Maximillians-Universität München.

de la Puente, J., Käser, M., Dumbser, M., Igel, H., 2007. An arbitrary high-order discontinuous Galerkin method for elastic waves on unstructured meshes-IV. Anisotropy. Geophys. J. Int. 169, 1210–1228. https://doi.org/10.1111/j.1365-246X.2007.03381.x.

Du, Q., Li, B., Hou, B., 2009. Numerical modeling of seismic wavefields in transversely isotropic media with a compact staggered-grid finite difference scheme. Appl. Geophys. 6, 42–49. https://doi.org/10.1007/s11770-009-0008-z.

Etienne, V., Chaljub, E., Virieux, J., Glinsky, N., 2010. An hp-adaptive discontinuous Galerkin finite-element method for 3-D elastic wave modelling. Geophys. J. Int. 183, 941–962. https://doi.org/10.1111/j.1365-246X.2010.04764.x.

Fletcher, R., Du, X., Fowler, P., 2009. Reverse time migration in tilted transversely isotropic (TTI) media. Geophysics 74, WCA179–WCA187. https://doi.org/10.1190/1.3269902.

Gao, H., Zhang, J., 2006. Parallel 3-D simulation of seismic wave propagation in heterogeneous anisotropic media: a grid method approach. Geophys. J. Int. 165, 875–888. https://doi.org/10.1111/j.1365-246X.2006.02946.x.

He, X.J., Yang, D.H., Wu, H., 2015. A weighted Runge-Kutta discontinuous Galerkin method for wavefield modeling. Geophys. J. Int. 200, 1389–1410. https://doi.org/10.1093/gji/ggu487.

He, X.J., Yang, D.H., Ma, X., 2020a. A weighted Runge-Kutta discontinuous Galerkin method for 3D acoustic and elastic wave-field modeling. Commun. Comput. Phys. 28, 372–400. https://doi.org/10.4208/cicp.OA-2018-0072.

He, X.J., Yang, D.H., Ma, X., Lang, C., 2019a. Dispersion-dissipation analysis of the triangle-based discontinuous Galerkin method for scalar wave equation. Geophys. J. Int. 218, 1174–1198. https://doi.org/10.1093/gji/ggz170.

He, X.J., Yang, D.H., Ma, X., Zhou, Y., 2019b. Symplectic interior penalty discontinuous Galerkin method for solving the seismic scalar wave equation. Geophysics 84, T133–T145. https://doi.org/10.1190/geo2018-0492.1.

He, X.J., Yang, D.H., Ma, X., Qiu, C.J., 2020b. A modified numerical-flux-based discontinuous Galerkin method for 2D wave propagations in isotropic and anisotropic media. Geophysics 85, T257–T273. https://doi.org/10.1190/GEO2019-0485.1.

Hesthaven, J.S., Warburton, T., 2007. Nodal Discontinuous Galerkin Methods: Algorithms, Analysis, and Applications. Springer.

Hestholm, S., 1999. Three-dimensional finite difference viscoelastic wave modelling including surface topography. Geophys. J. Int. 139, 852–878. https://doi.org/

10.1046/j.1365-246x.1999.00994.x.
Hestholm, S., Ruud, B., 2002. 3D free-boundary conditions for coordinate-transform finite-difference seismic modelling. Geophys. Prospect. 50, 463–474. https://doi.org/10.1046/j.1365-2478.2002.00327.x.
Hu, F.Q., Hussaini, M.Y., Rasitarinera, P., 1999. An analysis of the discontinuous Galerkin method for wave propagation problems. J. Comput. Phys. 151, 921–946. https://doi.org/10.1006/jcph.1999.6227.
Huang, J., Hu, T., Song, J., Li, Y., Yu, Z., Liu, L., 2022. A novel hybrid method based on discontinuous Galerkin method and staggered-grid method for scalar wavefield modelling with rough topography. Geophys. Prospect. 70, 441–458. https://doi.org/10.1111/1365-2478.13171.
Igel, H., Mora, P., Riollet, B., 1995. Anisotropic wave propagation through finite-difference grids. Geophysics 60, 1203–1216. https://doi.org/10.1190/1.1443849.
Käser, M., Dumbser, M., 2006. An arbitrary high-order discontinuous Galerkin method for elastic waves on unstructured meshes—I: the two-dimensional isotropic case with external source terms. Geophys. J. Int. 166, 855–877. https://doi.org/10.1111/j.1365-246X.2006.03051.x.
Kim, S., Yin, X.Y., Liang, K., 2018. Decomposition of stiffness matrix for TTI media. Prog. Geophys. 33, 644–652. https://doi.org/10.6038/pg2018BB0240.
Komatitsch, D., Tromp, J., 1999. Introduction to the spectral element method for three-dimensional seismic wave propagation: Geophys. J. Intell. 139, 806–822. https://doi.org/10.1046/j.1365-246x.1999.00967.x.
Lamb, H., 1904. On the propagation of tremors over the surface of an elastic solid. Proc. Roy. Soc. Lond. 72, 477–486. https://doi.org/10.1098/rsta.1904.0013.
Lan, H., Zhang, Z., 2011. Three-dimensional wave-field simulation in heterogeneous transversely isotropic medium with irregular free surface. Bull. Seismol. Soc. Am. 101, 1354–1370. https://doi.org/10.1785/0120100194.
Levy, M.N., Nair, R.D., Tufo, H.M., 2007. High-order Galerkin methods for scalable global atmospheric models. Comput. Geosci. 33, 1022–1035. https://doi.org/10.1016/j.cageo.2006.12.004.
Liu, Y., Sen, M.K., 2009. An implicit staggered-grid finite-difference method for seismic modelling. Geophys. J. Int. 179, 459–474. https://doi.org/10.1111/j.1365-246X.2009.04305.x.
Liu, Q., Zhang, J., Gao, H., 2017. Reverse-time migration from rugged topography using irregular, unstructured mesh. Geophys. Prospect. 65, 453–466. https://doi.org/10.1111/1365-2478.12415.
Moczo, P., Kristek, J., Galis, M., Chaljub, E., Etienne, V., 2011. 3-D finite-difference, finite-element, discontinuous-Galerkin and spectral-element schemes analysed for their accuracy with respect to P-wave to S-wave speed ratio. Geophys. J. Int. 187, 1645–1667. https://doi.org/10.1111/j.1365-246x.2011.05221.x.
Moczo, P., Kristek, J., Halada, L., 2000. 3D 4th-order staggered-grid finite-difference schemes: stability and grid dispersion. Bull. Seismol. Soc. Am. 90, 587–603. https://doi.org/10.1785/0119990119.
Modave, A., St-Cyr, A., Warburton, T., 2016. GPU performance analysis of a nodal discontinuous Galerkin method for acoustic and elastic models. Comput. Geosci. 91, 64–76. https://doi.org/10.1016/j.cageo.2016.03.008.
Nielsen, P., Berg, P., Skovgaard, O., 1994. Using the pseudospectral technique on curved grids for 2D acoustic forward modelling. Geophys. Prospect. 42 (4), 321–341. https://doi.org/10.1111/j.1365-2478.1994.tb00213.x.
Patra, A.K., Nichita, C.C., Bauer, A.C., Pitman, E.B., Bursik, M., Sheridan, M.F., 2006. Parallel adaptive discontinuous Galerkin approximation for thin layer avalanche modeling. Comput. Geosci. 32, 912–926. https://doi.org/10.1016/j.cageo.2005.10.023.
Qiu, C., Yang, D.H., He, X., Li, J., 2020. A weighted Runge-Kutta discontinuous Galerkin method for reverse time migration. Geophysics 85, S343–S355. https://doi.org/10.1190/geo2019-0193.1.
Rao, Y., Wang, Y., 2019. Dispersion and stability condition of seismic wave simulation in TTI media. Pure Appl. Geophys. 176, 1549–1559. https://doi.org/10.1007/s00024-018-2063-y.
Reed, W.H., Hill, T.R., 1973. Triangular Mesh Methods for the Neutron Transport Equation. Los Alamos Scientific Laboratory Report, LA-UR, pp. 73–479.
Rivière, B., 2008. Discontinuous Galerkin Methods for Solving Elliptic and Parabolic Equations: Theory and Implementation. Society for Industrial and Applied Mathematics.
Sethi, H., Shragge, J., Tsvankin, I., 2022. Tensorial elastodynamics for coupled acoustic/elastic anisotropic media: incorporating bathymetry. Geophys. J. Int. 228, 999–1014. https://doi.org/10.1093/gji/ggab374.
Shragge, J., 2014. Solving the 3D acoustic wave equation on generalized structured meshes: a finite-difference time-domain approach. Geophysics 79, T363–T378. https://doi.org/10.1190/geo2014-0172.1.
Shragge, J., Konuk, T., 2020. Tensorial elastodynamics for isotropic media. Geophysics 85, T359–T373. https://doi.org/10.1190/geo2020-0156.1.
Sun, Y.C., Zhang, W., Chen, X., 2016. Seismic-wave modeling in the presence of surface topography in 2D general anisotropic media by a curvilinear grid finite-difference method. Bull. Seismol. Soc. Am. 106, 1036–1054. https://doi.org/10.1785/0120150285.
Sun, Y.C., Zhang, W., Chen, X., 2018. 3D seismic wavefield modeling in generally anisotropic media with a topographic free surface by the curvilinear grid finite-difference method. Bull. Seismol. Soc. Am. 108, 1287–1301. https://doi.org/10.1785/0120170154.
Thomsen, L., 1986. Weak elastic anisotropy. Geophysics 51, 1954–1966. https://doi.org/10.1190/1.1442051.
Virieux, J., 1986. P-SV wave propagation in heterogeneous media: velocity-stress finite-difference method. Geophysics 51, 889–901. https://doi.org/10.1190/1.1442147.
Wang, L.C., Chang, X., Wang, Y.B., 2016. Forward modeling of pseudo P waves in TTI medium using staggered grid. Chin. J. Geophys. 59, 1046–1058. https://doi.org/10.6038/cjg20160325.
Wang, Z.Y., Huang, J.P., Liu, D.J., Li, Z.C., Yong, P., Yang, Z.J., 2019. 3D variable-grid full-waveform inversion on GPU. Petrol. Sci. 16, 1001–1014. https://doi.org/10.1007/s12182-019-00368-2.
Wu, G.C., Liang, K., Yin, X.Y., 2010. The analysis of phase velocity and polarization feature for elastic wave in TTI media. Chin. J. Geophys. 53, 1914~1923. https://doi.org/10.3969/j.issn.0001-5733.2010.08.017.
Xu, J., Hu, H., Liu, Q.H., Zhan, Q., Zhuang, M., 2021. Spectral element modeling of elastic wave propagation in an anisotropic background with discrete anisotropic fractures. Geophys. J. Int. 227, 832–848. https://doi.org/10.1093/gji/ggab226.
Yang, D.H., He, X.J., Ma, X., Zhou, Y.J., Li, J.S., 2016. An optimal nearly analytic discrete-weighted Runge-Kutta discontinuous Galerkin hybrid method for acoustic wavefield modeling. Geophysics 81, T251–T263. https://doi.org/10.1190/geo2015-0686.1.
Yang, D., Song, G., Lu, M., 2007. Optimally accurate nearly analytic discrete scheme for wave-field simulation in 3D anisotropic media. Bull. Seismol. Soc. Am. 97, 1557–1569. https://doi.org/10.1785/0120060209.
Zhang, W., Zhang, Z., Chen, X., 2012. Three-dimensional elastic wave numerical modelling in the presence of surface topography by a collocated-grid finite-difference method on curvilinear grids. Geophys. J. Int. 190, 358–378. https://doi.org/10.1111/j.1365-246X.2012.05472.x.
Zhu, J., Dorman, J., 2000. Two-dimensional, three-component wave propagation in a transversely isotropic medium with arbitrary-orientation–finite-element modelling. Geophysics 65, 934–942. https://doi.org/10.1190/1.1444789.